Enhanced photo-response of WS_2 photodetectors through interfacial defect engineering using TiO_2 interlayer

Yusin Pak[1,#], Woojin Park[2,#], Naresh Alaal[1], Yogeenth Kumaresan[3], S. Assa Aravindh [4], Somak Mitra[1], Bin Xin[1], Jung-Wook Min[2], Hyeonghun Kim[3], Namsoo Lim[3], Byungjin Cho[5], Gun-Young Jung[3], Muhammad M. Hussain[2], Iman S. Roqan[1*]*

[1]Physical Sciences and Engineering Division, King Abdullah University of Science and Technology (KAUST), Thuwal, 23955-6900, Saudi Arabia

[2]Computer Electrical Mathematical Science and Engineering, King Abdullah University of Science and Technology (KAUST), Thuwal, 23955-6900, Saudi Arabia

[3]School of Materials Science and Engineering, Gwangju Institute of Science and Technology (GIST), Gwangju, 61005, Republic of Korea

[4]Nano and Molecular Systems Research Unit, University of Oulu, 90014, Finland

[5]Department of Advanced Materials Engineering, Chungbuk National University, Cheongju, 28644, Republic of Korea

[#] *Equal contribution as first authors.*

*Corresponding Authors:

E-mail: muhammadmustafa.hussain@kaust.edu.sa, iman.roqan@kaust.edu.sa

KEYWORDS: tungsten disulfide, titanium dioxide, photodetector, atomic layer deposition, interfacial defect.

ABSTRACT

To develop a stable and reliable two-dimensional (2D) tungsten disulfide (WS_2)-based photodetector (PD), it is essential to address the issue of interfacial defects that are unavoidably formed at an interface between WS_2 and metal contact, as such defects can markedly deteriorate photo-response characteristics. In this work, this drawback is mitigated by adopting a facile technique for passivating a WS_2 surface with an ultrathin TiO_2 film. The TiO_2 interlayer is deposited on the 2D-WS_2 surface via twenty cycles of atomic layer deposition (ALD) prior to proceeding with photolithography and contact metal deposition. Advanced characterizations reveal that TiO_2/WS_2 PD exhibits enhanced photo-response compared to bare WS_2. Much higher photo-responsivity (~10 times higher at 1 mW/cm^2) and faster recovery (~124 times faster at 0.1 V) is obtained from TiO_2/WS_2 PDs relative to bare WS_2 PDs. The mechanism underlying the enhanced PD performance is faithfully demonstrated. The computational density functional theory (DFT) using Heyd-Scuseria-Ernzerhof (HSE) approach demonstrates the significant role of TiO_2/WS_2 interface in facilitating the charge transfer, and improving the PD performance compared to the bare device. This approach paves the way for developing reliable and high-performance 2D WS_2-based optoelectronic devices.

■ INTRODUCTION

Photodetectors (PDs), as essential elements of optoelectronic systems, are widely utilized in imaging, optical communications, and sensing applications.[1–7] Recently, two-dimensional (2D) materials with superior optoelectronic properties based on strong light–matter interaction[8] have attracted considerable attention of researchers and industry practitioners as next-generation photodetection platforms. These 2D materials are readily exfoliated or grown into atomically thin layers due to a weak Van der Waals force, facilitating their use in versatile optoelectronic devices requiring 2D material properties. In this regard, 2D graphene with a high carrier mobility and wide-band absorption spectrum has been actively studied. However, its zero bandgap and high transmittance (~97% in the visible range) are significant drawbacks for optoelectronic applications.[9–11] Consequently, graphene-like transition metal dichalcogenides (TMDCs),[12] in particular 2D-tungsten disulfide (WS_2), are potential candidates for high-performance PD development due to the existence of their bandgap. WS_2 has a high light extinction coefficient of $10^5 \sim 10^6$ cm^{-1}, a layer-dependent tunable bandgap of 1.3∼2.1 eV, and a large phonon-limited mobility of $> 10^3$ $cm^2/V \cdot s$ at room temperature, making it ideal for PD applications.[13–15] WS_2-based PDs exhibiting such excellent properties have yielded promising performance.[16–20] Furthermore, various device architectures have been studied to elicit new WS_2-based PD functionalities.[21–23] However, PDs based on 2D-WS_2 are still unstable for practical applications.

PD-based WS_2 performance degradation stems from numerous factors, many of which are related to the thermodynamically unstable properties of 2D materials.[24] During metal contact fabrication, interfacial defects are unavoidably introduced onto 2D material surfaces. Such defects on the metal contact interface facilitate adsorption of water or gas molecules, which can degrade photo-generation and carrier transport.[25,26] To overcome this issue, a technique for passivating a whole 2D molybdenum disulfide (MoS_2) device with a hafnium dioxide (HfO_2) thin film as a final fabrication step was recently reported.[27] This approach was shown to yield improved PD performance by preventing adsorption of undesired gas molecules onto the MoS_2 surface. However, it was ineffective in controlling interfacial defects between contact metal and photodetection material. Thus far, many studies related to interfacial engineering have been conducted, focusing on other 2D materials (e.g., graphene and MoS_2 platforms), due to which there is an evident paucity of studies on the interfacial defect control aimed at enhancing the WS_2 PD performance. However, the enhanced photo-response and optical properties of WS_2 functionalized by TiO_2 interlayer inserted below the metal contact and the effect of its interface with WS_2 have never been studied. In addition, the effect of TiO2/WS2 interface on the PD characteristics and enhancement mechanism have not been investigated yet.

In this work, we address this gap in extant research by passivating a surface of exfoliated WS_2 with an ultrathin titanium dioxide (TiO_2) interlayer through atomic layer deposition (ALD). Subsequent investigations demonstrate that WS_2 PDs with the TiO_2 interlayer exhibit enhanced photo-responsivity compared to bare WS_2 PDs as a reference. We also studied the PD photo-response characteristics to reveal the mechanism underlying the enhanced performance induced by the TiO_2 interlayer. Computational density functional theory (DFT) calculations using Heyd-Scuseria-Ernzerhof (HSE) functional further explain the mechanisms of the performance enhancement.

■ EXPERIMENTAL DETAILS

TiO_2 interlayer deposition via ALD process. WS_2 flakes were exfoliated and transferred onto a 200-nm-thick SiO_2/ 4-inch p-type Si wafer by using a 3M tape. One ALD cycle was performed at 200 ^{o}C under oxygen (O_2) plasma ambient, and subsequently was purged under argon

(Ar) plasma ambient (Oxford Instruments Equipment). Further ALD cycles were carried out until 5 nm thickness was attained. Ti precursors were bubbled from liquid titanium isopropoxide $Ti(OC_3H_7)_4$ at 40 ^oC before placing them into a reaction chamber. For further device optimization, post-annealing has been performed on the fabricated device. We carried out electrical measurements on WS_2 field effect transistors (FETs) under three annealing (at 200 °C for more than 2 hrs) conditions—ambient, in vacuum, and in vacuum maintained for 14 h—to examine the transfer characteristics, as shown in Figure S1 in Supporting Information. We found that the best results were obtained for the samples annealed in vacuum for 14 h, since the absorbed chemical species are removed, due to which field effect mobility improved from 3.48 $cm^2V^{-1}s^{-1}$ to 3.95 $cm^2V^{-1}s^{-1}$.

Photo-response analysis. Devices were connected to a Keithley 2400S by using probes and electrical feed-through. Electrical signals were recorded and monitored using a LabView software prepared for current−voltage (I−V) measurements. A white light, calibrated at 100 mW/cm^2, was generated by a solar simulator (AM 1.5G spectra, ReRa Solutions) and the devices were illuminated directly from the top. To modulate the power density (P_d), neutral-density (ND) filters with different transmittances (100, 40, 25, 15, 10, 1, 0.7, 0.3, and 0.1%) were used in combination. To precisely control every ON/OFF cycle, an automatic shutter was placed beneath the solar simulator window.

Raman spectra measurement. To excite the WS_2 samples, a 473 nm laser equipped with the Horiba Aramis Jobin Yvon micro-Raman system was used at room temperature. The focused laser power was 5 mW and the grating was 600 g mm^{-1}.

Computational details. The calculations related to a $2H-WS_2$ and WS_2/TiO_2 structures were carried out by adopting the DFT simulation, as implemented in the software package

VASP,[28,29] whereby Perdew-Burke-Ernzerhof approximation (PBE)[30] was adopted for an exchange correlational function. An electron–ion interaction was described by a projected-augmented wave approach. An orthorhombic unit cell was adopted to model a TiO_2/WS_2 heterostructure.[31] To form TiO_2/WS_2 interface, we considered a 1 × 3 × 1 2D lepidocrocite-type TiO_2 supercell on top of a 1 × 4 × 1 2D WS_2 supercell. The valence states included 3*p*, 4*s* and 3*d* for Ti; 5*p*, 6*s* and 5*d* for W; 2*s* and 2*p* states for O; and 3*s* and 3*p* for S. All atoms in the supercell were relaxed until force on each atom declined below 0.01 eV/Å and a total energy convergence of 10^{-5} eV was achieved. A plane wave cutoff energy of 500 eV was chosen. A Monkhorst *k*-point grid of 11 × 3 × 2 was adopted to sample the first Brillouin zone of the TiO_2/WS_2 heterostructure. A vacuum layer of more than 15 Å was subsequently considered in *z*-direction. In order to correct the bandgaps obtained from PBE, the HSE functional[32] was used, setting the Hartree-Fock Exchange mixing parameter to 0.13 and the PBE fraction to 0.87. This approach has been successfully used in prior studies to predict the bandgaps for 2D systems.[31] The effect of Van der Waals interactions was included by using DFT-D3 dispersion scheme.[33,34]

■ RESULTS AND DISCUSSION

Figure 1a depicts the facile process adopted in this study for fabricating a WS_2-based PD with an ultrathin TiO_2 interlayer. The multilayered WS_2 was exfoliated from a bulk WS_2 target before being transferred onto a 200 nm thick silicon dioxide (SiO_2)/heavily doped p-type silicon (Si) substrate. The thickness of the exfoliated WS_2 used for either PD or FET devices ranged from approximately 9 nm to 20 nm. After depositing the ultrathin TiO_2 interlayer through ALD cycles at 200 ^{o}C, photolithography, electron beam evaporation, and lift-off processes were sequentially carried out to form titanium (Ti) electrodes for source-and-drain contacts with a channel length and width of 5 μm and 140 μm, respectively. Note that the real channel width of the WS_2 device is determined by the WS_2 sample dimensions. For gate biasing, the same Ti was deposited on the back Si side of the substrate. Figure 1b shows a cross-sectional transmission electron microscopy (TEM) image of three layers comprising of Ti/TiO_2/WS_2. The spacing between two adjacent WS_2 layers along the [0001] direction at a hexagonal close-packed lattice was about 0.65 nm, as shown in the TEM image. The thickness of the ALD-processed TiO_2 interlayer was approximately 5 nm, on which the 60 nm thick Ti as the source and drain electrodes were deposited. In a previous report, the ultrathin TiO_2 interlayer (for transistor devices)[35] was found to be very effective in minimizing the formation of undesired defects—such as vacancies, dislocations, and edge boundaries at the interface between 2D and Ti—due to ordered stacking of diffused Ti and O atoms.

Atomic force microscopy (AFM) was carried out to examine WS_2 morphology and roughness. Figure 1c shows the AFM image of bare WS_2 with a thickness of ~9 nm and a good root mean square (RMS) value (1.3 nm) is revealed. Note that surface coverage is a critical issue when depositing an insulating material through ALD. According to the findings yielded by related studies,[36,37] depositing a 3-nm-thick TiO_2 is sufficient to fully and smoothly cover the WS_2 surface. Here, we opted for a 5-nm-thick TiO_2 layer, in consideration of an engineering deviation stemming from the equipment employed in this work.

To confirm the structural and chemical properties of the WS_2 samples after TiO_2 deposition, Raman spectroscopy was performed on the same WS_2 samples based on the optimized thickness. This measurement allowed us to examine the effect of TiO_2 on the quality of WS_2 samples. Figure 1d shows Raman spectra of a set of representative samples (TiO_2/WS_2 and bare WS_2). The characteristic peak of E_{2g} at ~357.3 cm^{-1} and A_{1g} at ~421.6 cm^{-1} originating from in-plane and out-of-plane vibrational mode,[38] respectively, are clearly visible in Figure 1d. No significant changes in the Raman spectra were observed after the TiO_2 deposition (Figure S2 in Supporting

Information), confirming that the initial WS_2 crystallinity was well maintained without stresses[39, 40] that might be induced by the high-temperature ALD process. This finding reveals that the deposited TiO_2 with the optimal thickness of 5 nm maintains the structural quality of the WS_2 samples.

To evaluate the TiO_2 effect on electrical properties, I−V characteristics were analyzed. This electrical measurement was carried out at room temperature and under normal atmosphere. Figure 2a and 2b show output characteristics of the bare WS_2 and the TiO_2/WS_2 device, respectively, under gate voltages (V_G) that were increased from -50 V to 20 V in 5 V steps. Prominent differences in both I−V behavior and series resistance (R_{SD}) were clearly observed for both devices. The drain current (I_D) of the bare WS_2 device failed to gradually increase with the V_G, and it barely approached 1 μA under the drain voltage (V_D) of 1 V (Figure 2a). However, as shown in Figure 2b, the I_D values of the TiO_2/WS_2 device increased linearly with the V_D and readily surpassed 1 μ A under the same V_D = 1 V, as its turn-on gate voltage is more negative than that of the bare WS_2 device. This substantial difference in the subthreshold electrical properties was attributed to the reduction in interfacial defects following TiO_2 deposition, which was further confirmed by performing a discharging test where a gate-stress was applied for 10 s at V_g = 20 V (Figure S1b in Supporting Information).

Although theoretically designing a metal−semiconductor (M−S) interface with ideal perfect materials can facilitate carrier transport, real devices possess an abnormally formed potential barrier in the interface due to the presence of interfacial defects, which causes a high contact resistance (R_C), thus deteriorating PD performance. Therefore, controlling the interfacial defects is an effective method of reducing the R_C sufficiently, while removing the need for trial-and-error experiments to find the optimal contact metal. A transfer characteristic was examined to compare the R_C values of FET devices based on both bare Ti/WS_2 and $Ti/TiO_2/WS_2$ during the subthreshold phase. Figure 2c clearly shows that the bare WS_2 device was governed by a bi-polar behavior,[41] whereas the TiO_2/WS_2 device showed a more unipolar n-type depletion behavior. The appearance of unipolar n-type mode is attributed to free electrons, which are generated by oxygen vacancies in TiO_2 and then transferred to WS_2,[42] thus enhancing the carrier generation in TiO_2/WS_2 PD as will be shown later. In this case, hole conductivity is suppressed and the Fermi energy level is de-pinned.[35,43] Therefore, the TiO_2/WS_2 device turned on at lower voltage (V_G = ~ -37 V), and I_D increased as V_G increased, and the I_D value saturated at a value exceeded 10^{-7} A under V_G = -20 V, due to the reduced R_C value after the TiO_2 deposition. However, In contrast to the TiO_2/WS_2 device, the I_D of the bare WS_2 device slowly decreased as the V_G approached -20 V, and the n-type depletion mode with ~3 orders of the ON/OFF ratio appeared.

Figure 2d shows a plot of field effect mobility (μ_{FE}) as a function of V_G. The μ_{FE} is an indicator of FET switching speed and was calculated using the following expression:

$$I_D = \frac{1}{2}\mu_{FE}C_{ox}\frac{W}{L}(V_G - V_{th})V_D; \qquad (1)$$

where C_{ox} denotes oxide capacitance, W represents channel width, L is channel length, and V_{th} is the threshold voltage. For bare WS_2 and the TiO_2/WS_2 devices, maximum μ_{FE} of 0.003 $cm^2/V{\cdot}s$ and 0.22 $cm^2/V{\cdot}s$ was measured at the V_G of approximately -10 V and -16 V, respectively, indicating an enhancement in the μ_{FE} value due to the insertion of TiO_2. These FET characteristics confirm the role of TiO_2 in enhancing the electrical properties of the TiO_2/WS_2 device, leading to higher photo-generation carrier density in TiO_2/WS_2 PDs compared to the bare PDs.

Figure 3a and 3b show normalized photo-responses of the bare WS_2 and TiO_2/WS_2 devices when subjected to various power density (P_d) values (defined as an incident light power per unit projected area), which were analyzed using our home-made measurement setup (Figure S3 in

Supporting Information). In the bare WS_2 device, photocurrent (I_{ph}) gradually increased and the recovery was incomplete even after 5 min, as shown in Figure 3b. On the other hand, the TiO_2/WS_2 device exhibited a gradual I_{ph} increase as well as fast recovery (within several seconds). The slow and incomplete recovery at a low voltage or in self-powered operation mode can be typically related to a long carrier lifetime and/or a small diffusion coefficient.[44] In the bare WS_2 device, the interfacial defects could trap photo-generated carriers, thus hindering their releasement into the electrodes. Similar FET and PD enhancement has been reported for TiO_2/MoS_2 device, for which faster switching and more stable recovery were observed compared to bare MoS_2 devcie.[43] Hence, we expect a similar beneficial effect on the stability of TiO_2/WS_2 devices.

To compare photo-response efficiencies, a photo-responsivity (R_{ph}) value, defined as a ratio of I_{ph} to incident light power, was calculated. As the white light illumination has recently been employed for revealing the broadband PD characteristics, due to its potential applicaitons,[45-47] as a part of this investigation, our devices were studied under both white light (Figure 3) and monochromatic light illumination at different wavelengths (Figure S4). As shown in Figure 3c, the R_{ph} values of the TiO_2/WS_2 device (e.g. 1.2 A/W at 1 mW/cm^2) exceeded those pertaining to the bare WS_2 device (e.g. 0.15 A/W at 1 mW/cm^2) under all P_d values applied for the measurements. We further investigated detectivity (D*) to assess the optical detection limit. The D* value of the WS_2/TiO_2 device (Figure S4a in Supporting Information) at 10 mW/cm^2 was $1.\ 1 \times 0^{11}$ Jones which is much higher than that of the bare WS_2 device (0.6×10^{11} Jones). This difference in D* values signifies efficient generation and releasement of electron–hole pairs under illumination. In addition, TiO_2/WS_2 devices exhibited higher external quantum efficiency (EQE) compared to bare WS_2 devices, especially in the UV and deep UV wavelength range, as shown in Figure S4b.

In general, the absolute amount of I_{ph} can be increased by bending the M−S energy band under applied voltages (Figure S5 in Supporting Information). However, this may cause an undesired dark current increase and/or a slow recovery because trap-assisted tunneling and thermionic emission[48] can occur through the interfacial defects as charge pathways.[49] To evaluate a voltage-dependent photo-response, three voltages (0.1, 0.5, and 1 V) were applied under illumination. As seen in Figure 3d, as the voltage increased, the bare WS_2 device exhibited a dark current increase $[(0.9\ \mathrm{nA})_{0.1V} \rightarrow (1.6\ \mathrm{nA})_{0.5V} \rightarrow (9\ \mathrm{nA})_{1V}]$ and the slower recovery behavior $[(62\ \mathrm{s})_{0.1V} \rightarrow (94\ \mathrm{s})_{0.5V} \rightarrow (247\ \mathrm{s})_{1V}$ for a 90% decay]. On the other hand, the TiO_2/WS_2 device showed insignificant changes in both dark current $[(0.3\ \mathrm{nA})_{0.1V} \rightarrow (0.6\ \mathrm{nA})_{0.5V} \rightarrow (1.5\ \mathrm{nA})_{1V}]$ and the recovery time $[(0.5\ \mathrm{s})_{0.1V} \rightarrow (2.5\ \mathrm{s})_{0.5V} \rightarrow (14.4\ \mathrm{s})_{1V}$ for the same 90% decay], as shown in Figure 3e. Thus, photo-responsivity of TiO_2/WS_2 PD was found to be ~10 times higher, while its recovery time was ~124 times faster compared to bare WS_2 PDs.

To elucidate our findings, we performed wavelength-dependent photo-response measurements on both bare WS_2 and enhanced TiO_2/WS_2 devices based on different TiO_2 and WS_2 thicknesses, as shown in Figure S6 in Supporting Information. Although a further in-depth study is required, a very slight increase (at ~350 nm) in R_{ph} (which does not affect the total photo-response) was observed in the wavelength range corresponding to UV radiation. This phenomenon is probably associated with surplus electron−hole pairs generated within a band of TiO_2 (Figure S6b in Supporting Information).

Figure 4a and 4b show transfer characteristics of the bare WS_2 PD and the TiO_2/WS_2 PD under various P_d values, respectively. Both devices yielded greater I_{ph} as the P_d increased. However, while the I_{ph} of the bare WS_2 device was unstable and exhibited severe fluctuations, the I_{ph} of the TiO_2/WS_2 device increased gradually by following a trajectory similar to that of the dark current.

The severe I_{ph} fluctuations of the bare WS_2 device indicate that photo-carriers are repeatedly trapped and recombined at the M−S interface, and this issue becomes more pronounced as either V_G or P_d increases. As a result, the I_{ph} values of the bare WS_2 device were smaller than those of the TiO_2/WS_2 device across all applied voltages (Figure 4c). Under 100 mW/cm^2, the bare WS_2 device produced 475 nA, whereas 700 nA was measured for the TiO_2/WS_2 device under 1 mW/cm^2. It is worth noting that we compared the samples of the same thickness and effective area.

Figure 4d and 4e show logarithm plots for the transfer characteristics of PD devices presented in Figure 4a and 4b, respectively. As indicated in Figure 2, the WS_2 device suffered a pronounced reduction in the drain current required to open the n-type channel, since the Fermi energy was pinned at the M−S interface due to the defect states. Under dark conditions, the bare WS_2 device turned on at the threshold voltage (V_{th}) of -26 V, while the TiO_2/WS_2 device opened the electron channel at the V_{th} of -30 V. Under illumination, as the P_d increased, the V_{th} became more negative in both devices, implying early formation of an electron channel by the photo-carriers (Figure S7 in Supporting Information).

To evaluate the channel opening efficiency, a subthreshold swing (SS) was calculated using the inversion of the subthreshold slope (Figure S8 in Supporting Information). The SS of the WS_2 device increased with the P_d, while it decreased in the TiO_2/WS_2 device. This finding indicates that the electron accumulation needed for the channel inversion is unstable in the bare WS_2 device due to the presence of trap states. [49,50]

To understand the mechanism underlying the enhanced photo-response of the TiO_2/WS_2 device, we hypothesized the band diagrams shown in Figure 5 and Figure S6a in Supporting Information. Typically, a thick multilayered WS_2 is an n-type material with a work function of ~5.3 eV, which is higher than ~4.3 eV of Ti, as shown in the flat-band model in Figure 5a. Due to the work function difference, both conduction and valence band of WS_2 would bend down toward the Ti side. Under a negative gate bias (Figure 5b), the electron accumulation needed to open an electron channel does not occur due to the metal/WS_2 interface in the bare WS_2 device. A positive gate voltage can elevate the Fermi energy beyond the conduction band edge of the WS_2, forming an electron channel (Figure 5c). Under illumination, for bare WS_2 PD, gate electric fields do not properly propagate and photo-generated carriers are trapped by defect states, thus hindering the I_{ph} increase. However, defect density is reduced by introducing a TiO_2 interlayer, as shown in Figure 5d. As a result, photo-carriers can be readily released to the electrodes even at a low voltage.

To elucidate the mechanism of the observed enhancements in the TiO_2/WS_2 device and to reveal the effect of the TiO_2/WS_2 interface in improving the photo-transport properties, DFT calculations were performed for 2H−WS_2, TiO_2, and TiO_2/2H−WS_2. It is known that the PBE functional underestimates the band gap values, whereas the HSE functional increases the calculated bandgap values, approaching the experimental values.[51,52] Thus, the PBE and the corrected HSE calculations were applied to the TiO_2/WS_2 interface, as well as the bare WS_2 and bare TiO_2.

The approach adopted when modeling the heterostructure that includes WS_2 and TiO_2 layers is shown in Figure 5e. The optimized lattice parameters of the 2D TiO_2 orthorhombic unit cell are 3.02 and 3.76 Å, and the WS_2 lattice constant is 3.18 Å. Table 1 presents the calculated bandgap values using PBE functional, including the corrected HSE values for bare WS_2, bare TiO_2 and WS_2/TiO_2 interface, showing that the bandgaps of freestanding WS_2 (TiO_2) based on PBE (HSE) are 1.78 (2.98) eV and 2.17 (3.81) eV, respectively. These values are in good agreement with the previously reported results, including experimental findings.[31,53] On the other hand, TiO_2/WS_2

possesses small bandgap (0.42 and 0.81 eV, according to PBE approximation and HSE functional, respectively) compared to the individual monolayers, as presented in Table 1.

In order to identify the origin of the bandgap reduction, projected density of states (PDOS) for WS_2 and TiO_2/WS_2 were calculated and the findings are presented in Figure 5f. The PDOS plot shows that, for WS_2, the valence band maximum (VBM) and conduction band minimum originate from W-*d* states. When TiO_2 interacts with the 2H−WS_2, Ti-*d* (dominant) and O-*p* (minor) orbitals not only modify the band edges of both valence band and conduction band, but also contribute to forming energy states within the bandgap, as shown in Figure 5f. The presence of those additional states improved the conductivity at the M−S interface. These theoretical results demonstrates that the TiO_2/WS_2 interface assisted in improving the transport of the photo-generated carriers and providing additional carrier density[54,55] as the fermi-level de-pinned in the TiO_2/WS_2 interface due to the small bandgap of TiO_2/WS_2.

■ CONCLUSIONS

In this work, we demonstrated that both photo-responsivity and recovery time can be markedly improved simply by depositing TiO_2 at the interface between the WS_2 and the Ti electrode. The TiO_2 interlayer was highly effective in resolving the issue of photo-carrier trapping at the M−S interface, which was verified through power- and voltage-dependent photo-response characterizations. Moreover, the origin of the enhancement was revealed by DFT calculations, demonstrating that the TiO_2/WS_2 interface bandgap facilitates both carrier transport and interface conductivity, thus enhancing the PD photo-response, whereas metal/WS_2 interface traps carriers, leading to performance degradation. This work paves the way for achieving reliable, practical, and reproducible PD performance without the need for finding an optimal contact metal. Furthermore, the findings reported here will aid researchers in finding suitable means of enhancing the performance of other 2D-based optoelectronic devices.

■ ASSOCIATED CONTENT

Supporting Information

The Supporting Information is available free of charge on the ACS Publications website at DOI: Response enhancement under annealing conditions. Discharging test for devcies. Raman spectra for WS_2 samples measured before and after the TiO_2 deposition. The setup for measuring photodetection characteristics. Detectivity vs. power for devices. Current−Voltage characteristics for devices. EQE of both devices. The Flat-band diagram between TiO_2 and Ti. Normalized photo-responses as the function of wavelengths for devices. Threshold voltages as a function of power density. Transfer characteristics of devices for subthreshold slope and subthreshold swing (SS) analyses.

■ AUTHOR INFORMATION

Corresponding Author

*E-mail: muhammadmustafa.hussain@kaust.edu.sa and * Email: iman.roqan@kaust.edu.sa

Author contrbution

Y Pak and W Park equally contributed to designing and conducting the experiments, and writing the manuscript cooperatively. Therefore, Y Pak and W Park shared the first authorship. All the authors approved the final version of the manuscript.

Notes

The authors declare no competing financial interest.

■ ACKNOWLEDGMENTS

Authors thank the King Abdullah University of Science and Technology (KAUST) for the financial support. Muhammad M. Hussain gratefully acknowledges the use of the grant funded by KAUST Office of Sponsored Research (OSR) under Award No. REP/1/2707-01-01. Iman S. Roqan gratefully acknowledge the use of the base fund No. BAS/1/1319-01-01and the KAUST super-computing facility for providing the computational resources.

REFERENCES

(1) Tang, L.; Kocabas, S. E.; Latif, S.; Okyay, A. K.; Ly-Gagnon, D. S.; Saraswat, K. C.; Miller, D. A. B. Nanometre-scale germanium photodetector enhanced by a near-infrared dipole antenna. *Nat. Photonics.* **2008,** *2*, 226-229.

(2) Flemban, T. H.; Haque, M. A.; Ajia, I.; Alwadai, N.; Mitra, S.; Wu, T.; Roqan, I. S. A Photodetector Based on p-Si/n-ZnO Nanotube Heterojunctions with High Ultraviolet Responsivity. ACS Appl. Mater. Interfaces **2017**, 9, 37120−37127.

(3) Mitra, S.; Aravindh, A.; Das, G.; Pak, Y.; Ajia, I.; Loganathan, K.; Di Fabrizio, E.; Roqan, I. S. High-Performance Solar-Blind Flexible Deep-UV Photodetectors Based on Quantum Dots Synthesized by Femtosecond-Laser Ablation. *Nano Energy* **2018**, 48, 551−559.

(4) de Arquer, F. P. G.; Armin, A.; Meredith, P.; Sargent, E. H. Solution-processed semiconductors for next-generation photodetectors. *Nat. Rev. Mater.* **2017,** *2*, 16100.

(5) Yao, J. D.; Yang, G. W. Flexible and High-Performance All-2D Photodetector for Wearable Devices. *Small* **2018,** *14*, 1704524.

(6) Xin, B.; Pak, Y.; Mitra, S.; Almalawi, D.; Alwadai, N.; Zhang, Y.; Roqan, I. S. Self-Patterned CsPbBr3 Nanocrystals for High-Performance Optoelectronics. *ACS Appl. Mater. Interfaces* **2019**, 11, 5223-5231.

(7) Yao, J.; Zheng, Z.; Yang, G. All ‐ Layered 2D Optoelectronics: A High ‐ Performance UV–Vis–NIR Broadband SnSe Photodetector with Bi_2Te_3 Topological Insulator Electrodes. *Adv. Funct. Mater.* **2017**, *27*, 1701823.

(8) Britnell, L.; Ribeiro, R. M.; Eckmann, A.; Jalil, R.; Belle, B. D.; Mishchenko, A.; Kim, Y. J.; Gorbachev, R. V.; Georgiou, T.; Morozov, S. V.; Grigorenko, A. N.; Geim, A. K.; Casiraghi, C.; Castro Neto, A. H.; Novoselov, K. S. Strong Light-Matter Interactions in

Heterostructures of Atomically Thin Films. *Science* **2013,** *340*, 1311-1314.

(9) Zhang, Y. Z.; Liu, T.; Meng, B.; Li, X. H.; Liang, G. Z.; Hu, X. N.; Wang, Q. J. Broadband high photoresponse from pure monolayer graphene photodetector. *Nat. Commun.* **2013,** *4*, 1811.

(10) Mueller, T.; Xia, F. N. A.; Avouris, P. Graphene Photodetectors for High-Speed Optical Communications. *Nat. Photonics* **2010**, *4*, 297–301.

(11) Nair, R. R.; Blake, P.; Grigorenko, A. N.; Novoselov, K. S.; Booth, T. J.; Stauber, T.; Peres, N. M. R.; Geim, A. K. Fine Structure Constant Defines Visual Transparency of Graphene. *Science* **2008**, *320*, 1308.

(12) Wang, Q. H.; Kalantar-Zadeh, K.; Kis, A.; Coleman, J. N.; Strano, M. S. Electronics and optoelectronics of two-dimensional transition metal dichalcogenides. *Nat. Nanotechnol.* **2012,** *7*, 699-712.

(13) Zhao, W. J.; Ghorannevis, Z.; Chu, L. Q.; Toh, M. L.; Kloc, C.; Tan, P. H.; Eda, G. Evolution of Electronic Structure in Atomically Thin Sheets of WS_2 and WSe_2. *ACS Nano* **2013,** *7*, 791-797.

(14) Palummo, M.; Bernardi, M.; Grossman, J. C. Exciton Radiative Lifetimes in Two-Dimensional Transition Metal Dichalcogenides. *Nano Lett.* **2015,** *15*, 2794-2800.

(15) Bernardi, M.; Palummo, M.; Grossman, J. C. Extraordinary Sunlight Absorption and One Nanometer Thick Photovoltaics Using Two-Dimensional Monolayer Materials. *Nano Lett.* **2013**, *13*, 3664–3670.

(16) Zeng, L. H.; Tao, L. L.; Tang, C. Y.; Zhou, B.; Long, H.; Chai, Y.; Lau, S. P.; Tsang, Y. H. High-Responsivity UV-Vis Photodetector Based on Transferable WS_2 Film Deposited by Magnetron Sputtering. *Sci. Rep.* **2016**, *6*, 20343

(17) Huo, N. J.; Yang, S. X.; Wei, Z. M.; Li, S. S.; Xia, J. B.; Li, J. B. Photoresponsive and Gas Sensing Field-Effect Transistors Based on Multilayer WS_2 Nanoflakes. *Sci. Rep.* **2014**, *4*, 5209.

(18) Perea-Lopez, N.; Elias, A. L.; Berkdemir, A.; Castro-Beltran, A.; Gutierrez, H. R.; Feng, S. M.; Lv, R. T.; Hayashi, T.; Lopez-Urias, F.; Ghosh, S.; Muchharla, B.; Talapatra, S.; Terrones, H.; Terrones, M. Photosensor Device Based on Few-Layered WS_2 Films. *Adv. Funct. Mater.* **2013,** *23*, 5511-5517.

(19) Yao, J. D.; Zheng, Z. Q.; Shao, J. M.; Yang, G. W. Stable, Highly-Responsive and Broadband Photodetection Based on Large-Area Multilayered WS_2 Films Grown by Pulsed-Laser Deposition. *Nanoscale* **2015**, *7*, 14974–14981.

(20) Yao, J. D.; Zheng, Z. Q.; Yang, G. W. Layered-material WS_2/topological insulator Bi_2Te_3 heterostructure photodetector with ultrahigh responsivity in the range from 370 to 1550 nm. *J. Mater. Chem. C* **2016,** *4*, 7831-7840.

(21) Ma, C.; Shi, Y. M.; Hu, W. J.; Chiu, M. H.; Liu, Z. X.; Bera, A.; Li, F.; Wang, H.; Li, L. J.; Wu, T. Heterostructured $WS_2/CH_3NH_3PbI_3$ Photoconductors with Suppressed Dark Current and Enhanced Photodetectivity. *Adv. Mater.* **2016,** *28*, 3683-3689.

(22) Yu, W. J.; Liu, Y.; Zhou, H. L.; Yin, A. X.; Li, Z.; Huang, Y.; Duan, X. F. Highly efficient gate-tunable photocurrent generation in vertical heterostructures of layered materials. *Nat. Nanotechnol.* **2013,** *8*, 952-958.

(23) Yu, Y.; Zhang, Y. T.; Song, X. X.; Zhang, H. T.; Cao, M. X.; Che, Y. L.; Dai, H. T.; Yang, J. B.; Zhang, H.; Yao, J. Q. PbS-Decorated WS_2 Phototransistors with Fast Response. *ACS Photonics* **2017,** *4*, 950-956.

(24) Das, S.; Robinson, J. A.; Dubey, M.; Terrones, H.; Terrones, M. Beyond Graphene:

Progress in Novel Two-Dimensional Materials and van Der Waals Solids. *Annu. Rev. Mater. Res.* **2015**, *45*, 1–27.

(25) Yue, Q.; Shao, Z. Z.; Chang, S. L.; Li, J. B. Adsorption of gas molecules on monolayer MoS_2 and effect of applied electric field. *Nanoscale Res. Lett.* **2013,** *8*, 425.

(26) Addou, R.; Colombo, L.; Wallace, R. M. Surface Defects on Natural MoS_2. *ACS Appl. Mater. Interfaces* **2015,** *7*, 11921-11929.

(27) Kufer, D.; Konstantatos, G. Highly Sensitive, Encapsulated MoS_2 Photodetector with Gate Controllable Gain and Speed. *Nano Lett.* **2015,** *15*, 7307-7313.

(28) Kresse, G.; Hafner, J. Ab initio molecular dynamics for liquid metals. *Phys. Rev. B Condens. Matter.* **1993,** *47*, 558-561

(29) Kresse, G.; Furthmuller, J. Efficient iterative schemes for ab initio total-energy calculations using a plane-wave basis set. *Phys. Rev. B.* **1996,** *54*, 11169-11186.

(30) Perdew, J. P.; Burke, K.; Ernzerhof, M. Generalized Gradient Approximation Made Simple. *Phys. Rev. Lett.* **1996**, *77*, 3865.

(31) Li, Y.; Cai, C.; Sun, B.; Chen, J. Novel Electronic Properties of 2D MoS_2 /TiO_2 van Der Waals Heterostructure. *Semicond. Sci. Technol.* **2017**, *32*, 105011.

(32) Paier, J.; Marsman, M.; Hummer, K.; Kresse, G.; Gerber, I. C.; Ángyán, J. G. Screened Hybrid Density Functionals Applied to Solids. *J. Chem. Phys.* **2006**, *124*, 154709.

(33) Grimme, S.; Ehrlich, S.; Goerigk, L. Effect of the Damping Function in Dispersion Corrected Density Functional Theory. *J. Comput. Chem.* **2011**, *32*, 1456–1465.

(34) Grimme, S.; Antony, J.; Ehrlich, S.; Krieg, H. A Consistent and Accurate *Ab Initio* Parametrization of Density Functional Dispersion Correction (DFT-D) for the 94 Elements H-Pu. *J. Chem. Phys.* **2010**, *132*, 154104.

(35) Park, W.; Kim, Y.; Jung, U.; Yang, J. H.; Cho, C.; Kim, Y. J.; Hasan, S. M. N.; Kim, H. G.; Lee, H. B. R.; Lee, B. H. Complementary Unipolar WS_2 Field-Effect Transistors Using Fermi-Level Depinning Layers. *Adv. Electron. Mater.* **2016,** *2*, 1500278.

(36) Kobayashi, M.; Kinoshita, A.; Saraswat, K.; Wong, H. -S.; Nishi, Y. Fermi Level Depinning in Metal/Ge Schottky Junction for Metal Source/Drain Ge Metal-Oxide-Semiconductor Field-Effect-Transistor Application. *J. Appl. Phys.* **2009**, *105*, 23702.

(37) Kim, Y. J.; Park, W.; Yang, J. H.; Kim, Y.; Lee, B. H. Contact Resistance Reduction of WS_2 FETs Using High-Pressure Hydrogen Annealing. *IEEE J. Electron. Devi.* **2018,** *6*, 164-168.

(38) Berkdemir, A.; Gutierrez, H. R.; Botello-Mendez, A. R.; Perea-Lopez, N.; Elias, A. L.; Chia, C. I.; Wang, B.; Crespi, V. H.; Lopez-Urias, F.; Charlier, J. C.; Terrones, H.; Terrones, M. Identification of Individual and Few Layers of WS_2 using Raman Spectroscopy. *Sci. Rep.* **2013,** *3*, 1755.

(39) Muhammed, M. M.; Alwadai, N.; Lopatin, S.; Kuramata, A.; Roqan, I. S. High-Efficiency InGaN/GaN Quantum Well-Based Vertical Light-Emitting Diodes Fabricated on β-Ga2O3 Substrate. *ACS Appl. Mater. Interfaces* 2017, 9, 39, 34057-34063.

(40) Wu, F.; Sun, H.; Ajia, I. A.; Roqan, I. S.; Zhang, D.; Dai, J.; Chen, C.; Chuan, Z.; Feng, Li, X. Significant internal quantum efficiency enhancement of GaN/AlGaN multiple quantum wells emitting at ~350 nm via step quantum well structure design. *J. Phys. D.: Appl. Phys.* 2017, 50, 245101.

(41) Khalil, H. M. W.; Khan, M. F.; Eom, J.; Noh, H. Highly Stable and Tunable Chemical Doping of Multi layer WS_2 Field Effect Transistor: Reduction in Contact Resistance. *ACS Appl. Mater. Interfaces* **2015,** *7*, 23589-23596.

(42) Nie, X. L.; Zhuo, S. P.; Maeng, G.; Sohlberg, K. Doping of TiO_2 Polymorphs for Altered Optical and Photocatalytic Properties. *Int. J. Photoenergy.* **2009**, *2009*, 294042.

(43) Pak, Y.; Park, W.; Mitra, S.; Devi, A. A. S.; Loganathan, K.; Kumaresan, Y.; Kim, Y.; Cho, B.; Jung, G. Y.; Hussain, M. M.; Roqan, I. S. Enhanced Performance of MoS_2 Photodetectors by Inserting an ALD-Processed TiO_2 Interlayer. *Small* **2018,** *14*, 1703176.

(44) Goldberg, Y. A. Semiconductor near-ultraviolet photoelectronics. *Semicond. Sci. Tech.* **1999,** 14, 41-60.

(45) Asuo, I. M.; Fourmont, P.; Ka, I.; Gedamu, D.; Bouzidi, S.; Pignolet, A.; Nechache, R.; Cloutier, S. G. Highly Efficient and Ultrasensitive Large-Area Flexible Photodetector Based on Perovskite Nanowires. *Small* **2019**, 15, 1804150.

(46) Mondal, S.; Dutta, K.; Dutta, S.; Jana, D.; Kelly, A. G.; De, S. Efficient Flexible White-Light Photodetectors Based on BiFeO3 Nanoparticles. ACS Appl. Nano Mater. **2018**, 1 (2), 625– 631.

(47). Kim, J., Kwon, S. M., Kang, Y. K., Kim, Y. H., Lee, M. J., Han, K., Facchetti, A., Kim, M.G., Park, S. K., A skin-like two-dimensionally pixelized full-color quantum dot photodetector. Sci. Adv. 2019, 5, eaax8801.

(48) Alfaraj, N.; Mitra, S.; Wu, F.; Ajia, I. A.; Janjua, B.; Prabaswara, A.; Aljefri, R. A.; Sun, H.; Ng, T. K.; Ooi, B. S.; Roqan, I. S.; Li, X. Photoinduced Entropy of InGaN/GaN p-i-n Double-Heterostructure Nanowires. *Appl. Phys. Lett.* 2017, 110, 161110.

(49) Takei, K.; Hashimoto, S.; Sun, J.; Zhang, X.; Asada, S.; Xu, T. Y.; Matsukawa, T.; Masahara, M.; Watanabe, T. ON current enhancement of nanowire Schottky barrier tunnel field effect transistors. *Jpn. J. Appl. Phys.* **2016,** *55*, 04ed07.

(50) Flemban, T. H.; Sequeira, M. C.; Zhang, Z.; Venkatesh, S.; Alves, E.; Lorenz, K.; Roqan,

I. S. A Identifying the influence of the intrinsic defects in Gd-doped ZnO thin-films. *J. Appl. Phys.* 2016, 119, 065301.

(51) Carignano, M. A.; Aravindh, S. A.; Roqan, I. S.; Even, J.; Katan, C. Critical Fluctuations and Anharmonicity in Lead Iodide Perovskites from Molecular Dynamics Supercell Simulations. *J. Phys. Chem. C* 2017, 121, 20729– 20738.

(52) Bantounas, I.; Singaravelu, V.; Roqan, I. S.; Schwingenschlögl, U. Structural and Magnetic Properties of Gd-Doped ZnO. *J. Mater. Chem. C* 2014, 2, 10331– 10336.

(53) Li, Y. G.; Li, Y. L.; Sa, B. S.; Ahuja, R. Review of Two-Dimensional Materials for Photocatalytic Water Splitting from a Theoretical Perspective. *Catal. Sci. Technol.* **2017**, *7*, 545–559.

(54) Aravindh, S. D. A.; Schwingenschlögl, U.; Roqan, I. S. Defect induced d0 ferromagnetism in a ZnO grain boundary. *J. Chem. Phys.* 2015, 143, 224703.

(55) Zhang, Z.; Schwingenschlögl, U.; Roqan, I. S. Possible mechanism for d0 ferromagnetism mediated by intrinsic defects. *RSC Adv.* 2014, 4, 50759– 50764.

■ FIGURE CAPTIONS

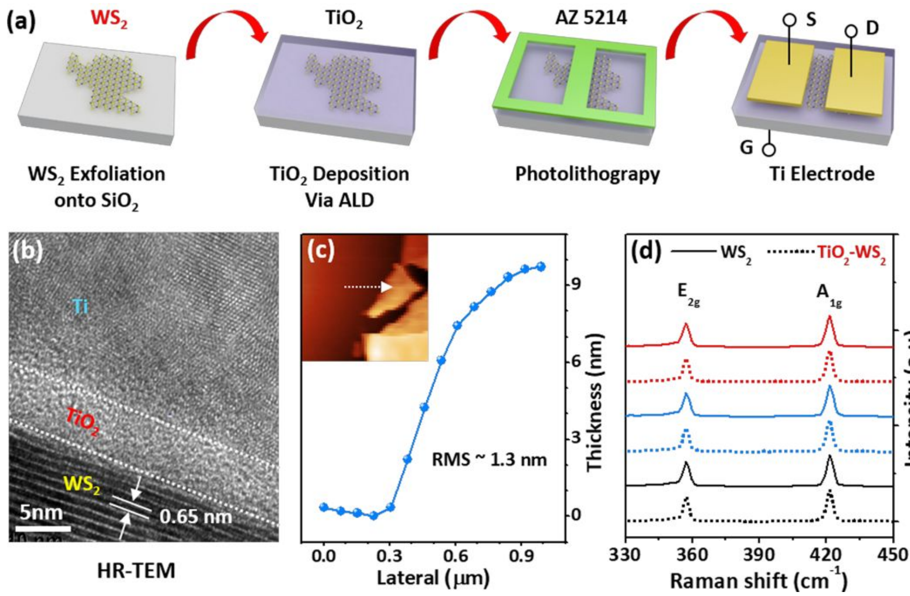

Figure 1. (a) The facile process adopted for fabricating the TiO_2/WS_2 devices. (b) The cross-sectional TEM image for the Ti-TiO_2-WS_2 device structure. (c) AFM image of a WS_2 flake. (d) Raman spectra of the representative WS_2 samples before and after ALD-processed TiO_2 deposition.

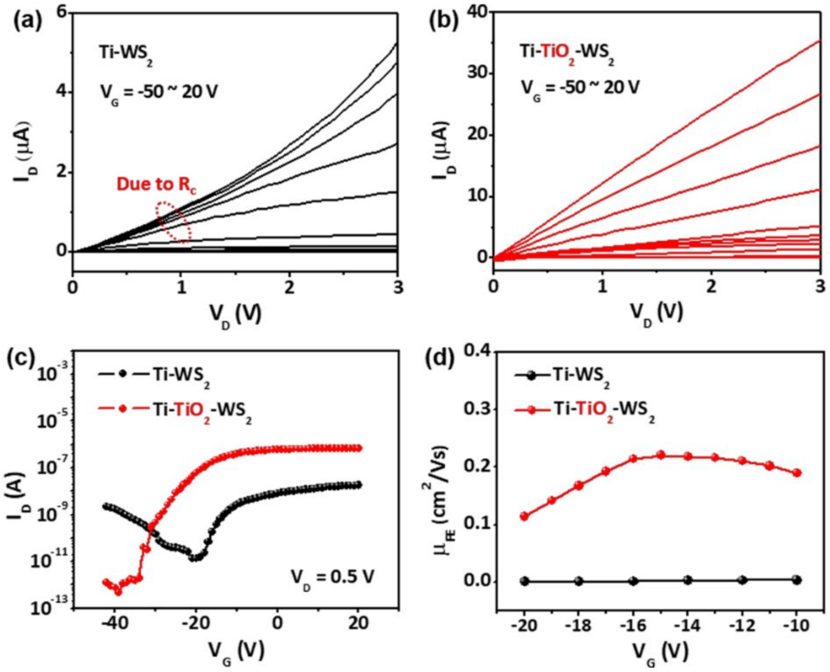

Figure 2. Output characteristics of (a) the bare WS_2 device and (b) the TiO_2/WS_2 device; (c) The transfer characteristic at V_D of 0.5 V and (d) the extracted mobility of both devices.

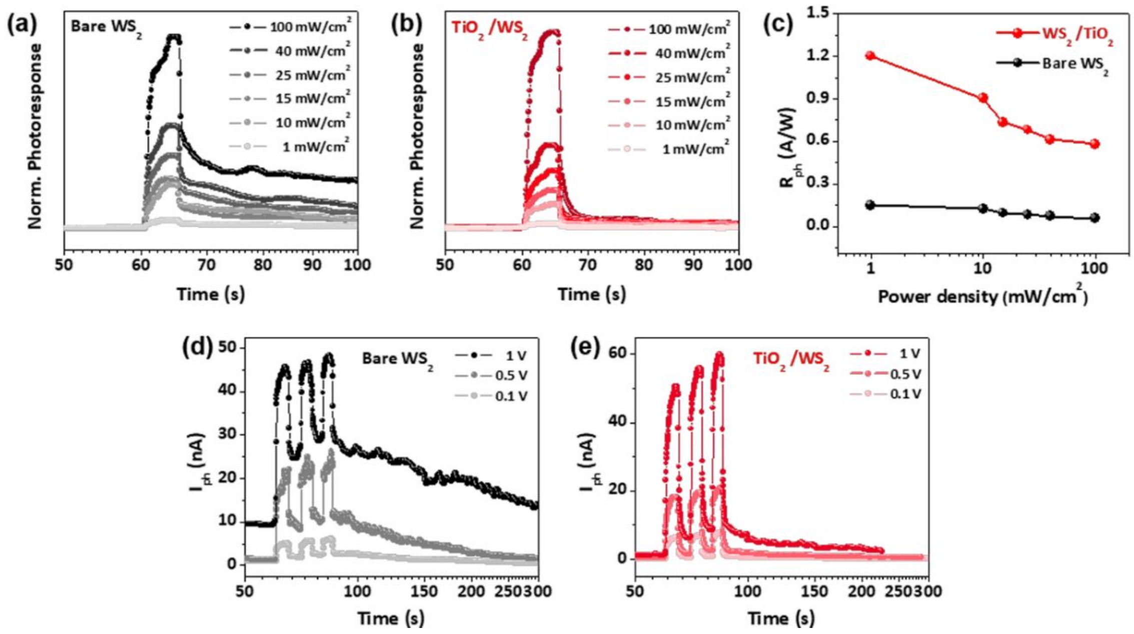

Figure 3. Photo-response characteristics of the bare WS_2 and the TiO_2/WS_2 device. Normalized photo-responses of (a) the WS_2 and (b) the TiO_2/WS_2 device under various P_d values and (c) their corresponding photo-responsivities. Photocurrents of (d) the WS_2 and (e) the TiO_2/WS_2 device under various voltages.

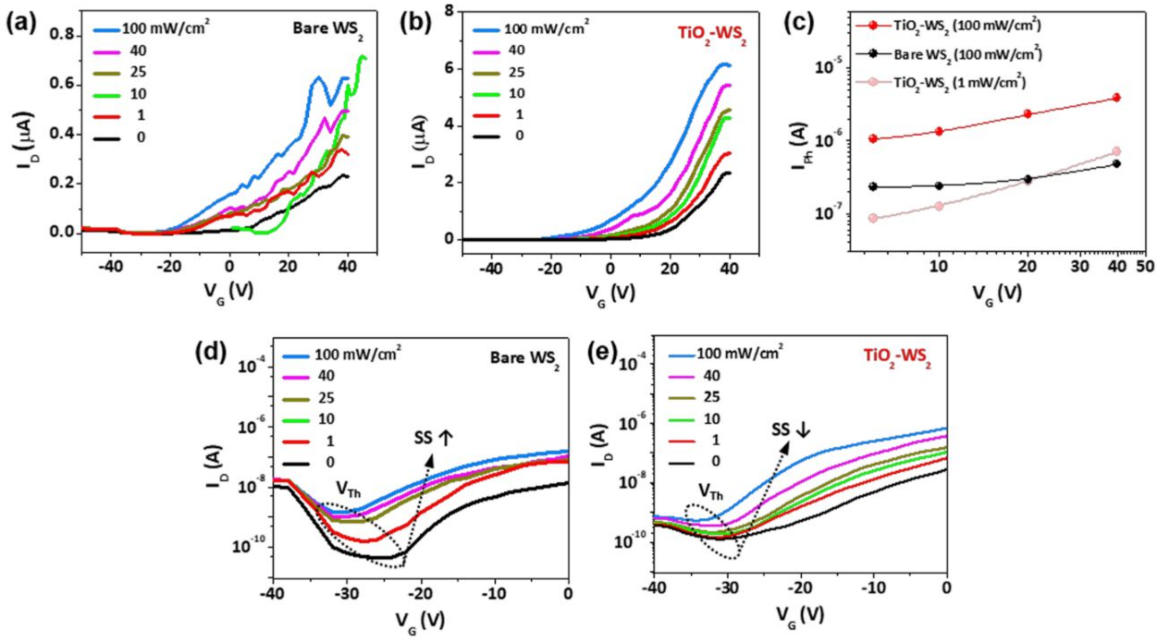

Figure 4. Enhanced photo-response under different gate voltages. The I_D−V_G transfer characteristics of (a) the WS_2 and (b) the TiO_2/WS_2 device under various P_d values, and (c) produced I_{ph} values for samples with the same WS2 thickness. Logarithmic I_D−V_G plots showing a subthreshold drain current of (d) the WS_2 and (e) the TiO_2/WS_2 device.

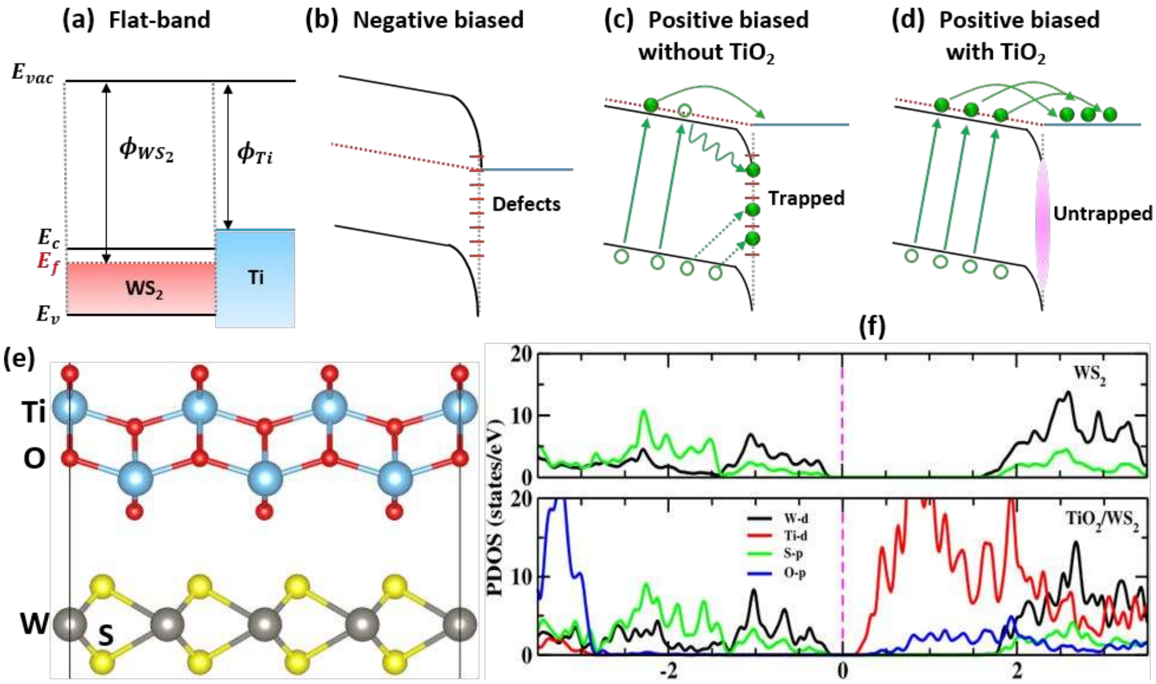

Figure 5. The theoretical and computational understanding for the enhanced photo-response of the TiO_2/WS_2 device. The band diagram for (a) flat-band, (b) negative bias, (c) positive bias without the TiO_2 interlayer, and (d) positive biased with the TiO_2 interlayer. (e) The heterostructure of TiO_2/WS_2 supercell and (f) the calculated total and projected DOS of TiO_2/WS_2 using DFT approach.

Table 1. Band gaps of WS_2, TiO_2, WS_2/TiO_2 structures. All the band gap values are in eV.

	WS_2	**TiO_2**	**TiO_2/WS_2**
PBE	1.78	2.98	0.43
HSE	2.17	3.8	0.81

Table of contents

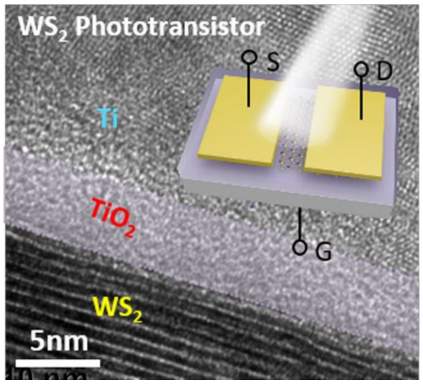

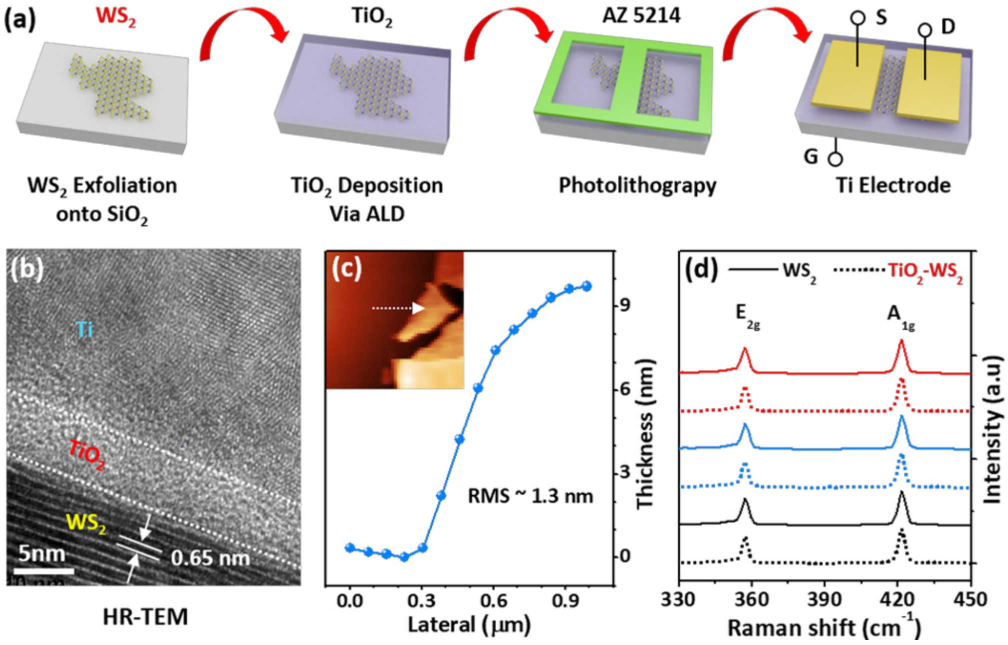

Figure 1

85x54mm (300 x 300 DPI)

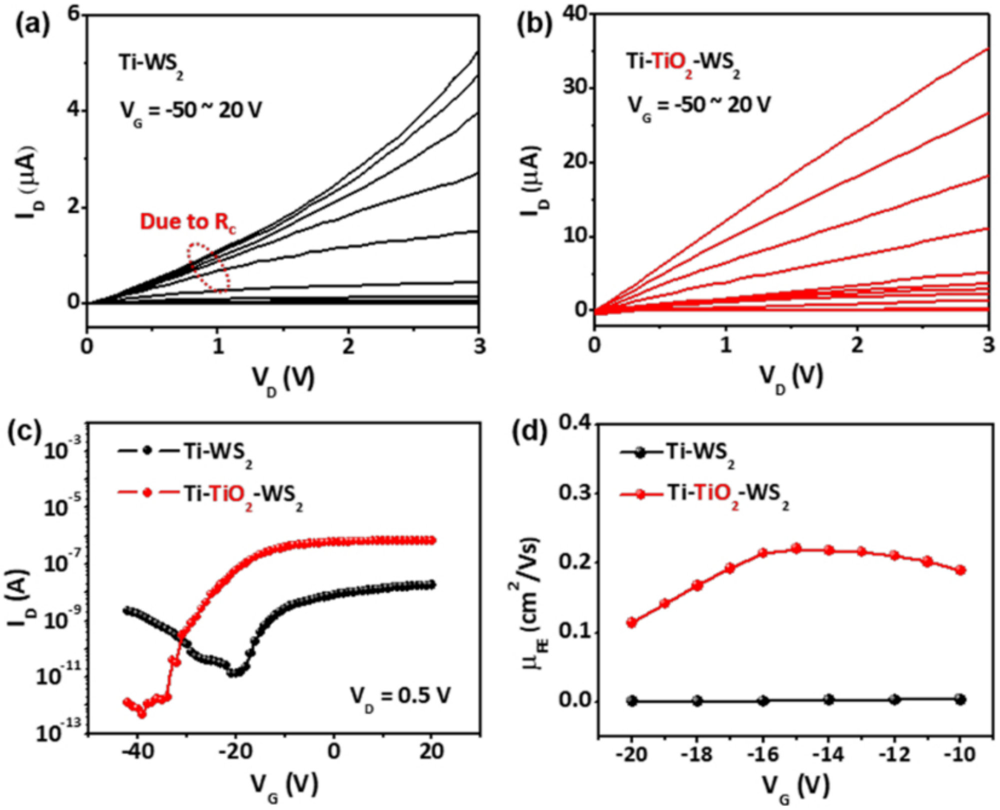

Figure 2

70x57mm (300 x 300 DPI)

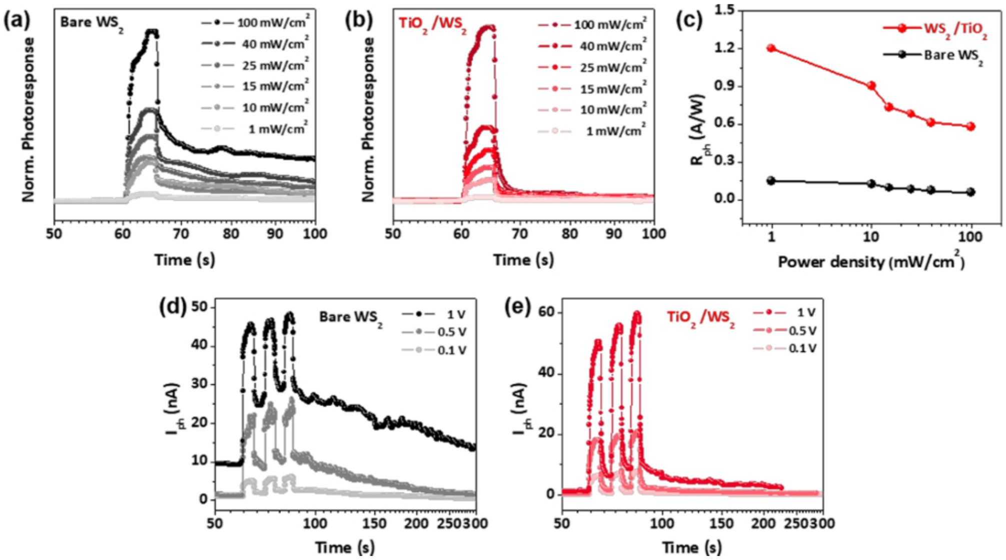

Figure 3

85x46mm (300 x 300 DPI)

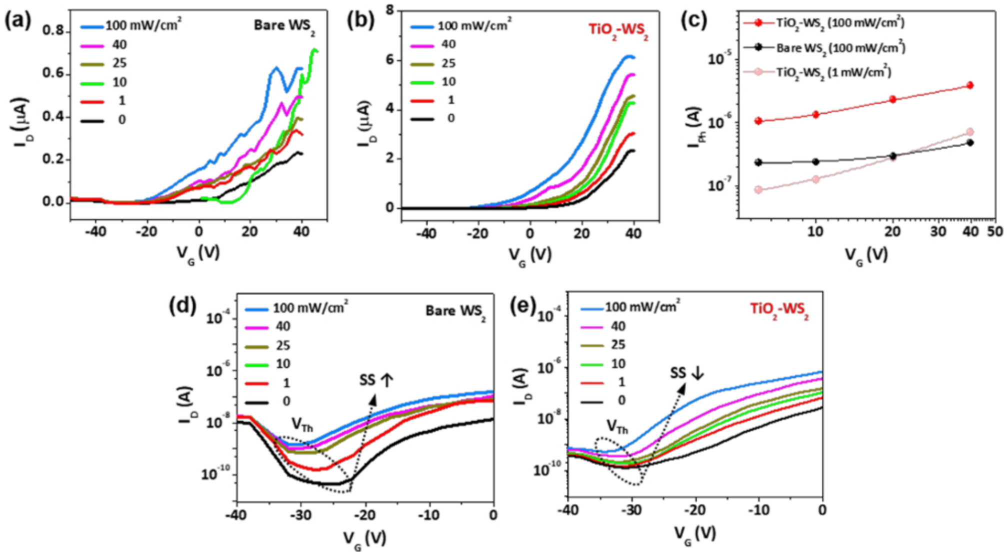

Figure 4

85x46mm (300 x 300 DPI)

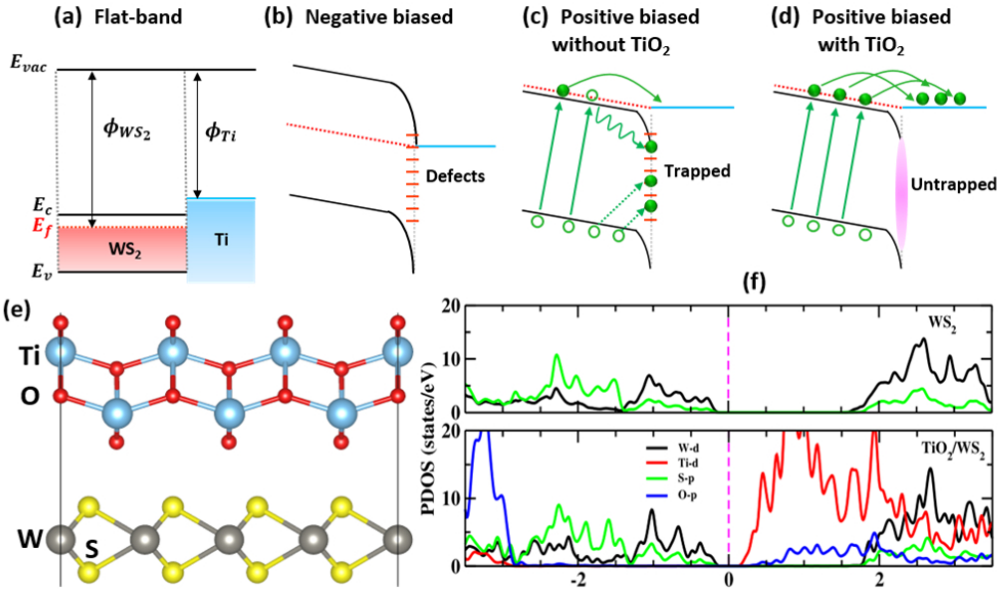

Figure 5

85x49mm (300 x 300 DPI)

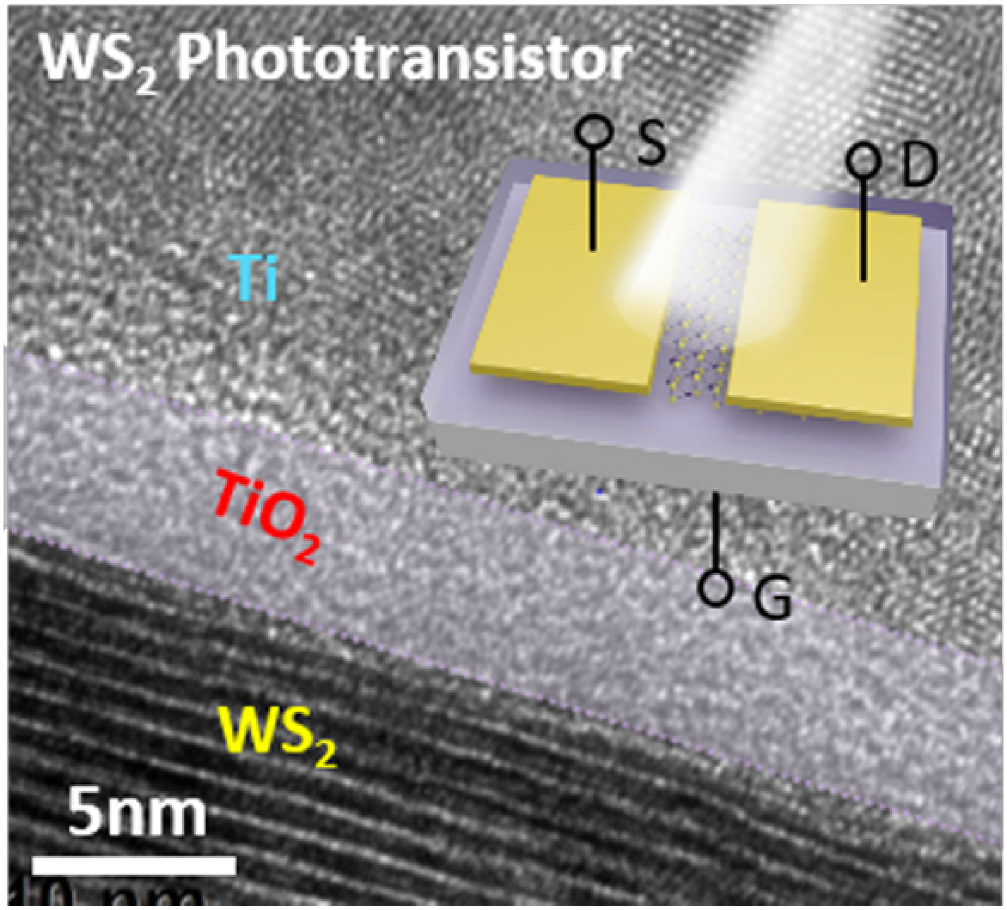

TOC

49x44mm (300 x 300 DPI)